Bioactive Materials 15 (2022) 382–391

Contents lists available at ScienceDirect

Bioactive Materials

journal homepage: www.keaipublishing.com/en/journals/bioactive-materials

Evaluating metallic artefact of biodegradable magnesium-based implants in magnetic resonance imaging

Jonathan Espiritu [a,*], Mostafa Berangi [b,c,d], Christina Yiannakou [e], Eduarda Silva [f], Roberto Francischello [g,h], Andre Kuehne [b], Thoralf Niendorf [b,c,d], Sören Könneker [c], Regine Willumeit-Römer [i], Jan-Marten Seitz [a]

[a] Syntellix AG, Hannover, Germany
[b] MRI.TOOLS GmbH, Berlin, Germany
[c] Charité – Universitätsmedizin Berlin, Corporate Member of Freie Universität Berlin and Humboldt Universität zu Berlin, Berlin, Germany
[d] Berlin Ultrahigh Field Facility (B.U.F.F.), Max-Delbrueck Center for Molecular Medicine in the Helmholtz Association, Berlin, Germany
[e] Hannover Medical School, Hannover, Germany
[f] Institute of Clinical Physiology, National Research Council, Pisa, Italy
[g] Chemistry and Industrial Chemistry Department, Università di Pisa, Via Moruzzi 13, Pisa, Italy
[h] Fondazione Toscana Gabriele Monasterio, Via Moruzzi 1, Pisa, Italy
[i] Institute for Materials Research, Helmholtz Zentrum Hereon, Geesthacht, Germany

ARTICLE INFO

Keywords:
Magnetic resonance imaging
Magnesium
Biodegradable implants
Medical imaging
Translational medicine

ABSTRACT

Magnesium (Mg) implants have shown to cause image artefacts or distortions in magnetic resonance imaging (MRI). Yet, there is a lack of information on how the degradation of Mg-based implants influences the image quality of MRI examinations. In this study, Mg-based implants are analysed *in vitro, ex vivo,* and in the clinical setting for various magnetic field strengths with the aim to quantify metallic artefact behaviour. *In vitro* corroded Mg-based screws and a titanium (Ti) equivalent were imaged according to the ASTM F2119. Mg-based and Ti pins were also implanted into rat femurs for different time points and scanned to provide insights on the influence of soft and hard tissue on metallic artefact. Additionally, MRI data of patients with scaphoid fractures treated with CE-approved Mg-based compression screws (MAGNEZIX®) were analysed at various time points post-surgery. The artefact production of the Mg-based material decreased as implant material degraded in all settings. The worst-case imaging scenario was determined to be when the imaging plane was selected to be perpendicular to the implant axis. Moreover, the Mg-based implant outperformed the Ti equivalent in all experiments by producing lower metallic artefact ($p < 0.05$). This investigation demonstrates that Mg-based implants generate significantly lower metallic distortion in MRI when compared to Ti. Our positive findings suggest and support further research into the application of Mg-based implants including post-operative care facilitated by MRI monitoring of degradation kinetics and bone/tissue healing processes.

1. Introduction

Traditional permanent orthopaedic implants have shown to cause inflammatory responses [1] in addition to further refracture risk [2]. These inappropriate bodily reactions and mechanical failures suggest that other solutions be investigated for temporary bone support, such as magnesium (Mg)- based alloy materials. The ability to safely degrade *in vivo* as a load-bearing implant material is arguably the most attractive property [3–5]. The similar elastic modulus and densities between Mg alloys and natural bone prevent negative mechanical conditions such as stress-shielding [6]. Recognizing the increasing usage of Mg material in the clinical setting magnetic resonance imaging (MRI) presents a viable diagnostic imaging modality for the examination of the degradation status of biodegradable implants and for the study of the implant/tissue interface. MRI is a mainstay of today's diagnostic imaging due to its ability to provide excellent soft tissue contrast at high spatial resolution [7–9]. Computed tomography (CT) is widely used in clinical practice to image bone fractures and corresponding implants. However, CT provides little information on soft tissue processes. The use of ionising

Peer review under responsibility of KeAi Communications Co., Ltd.
* Corresponding author.
E-mail address: espiritu@syntellix.com (J. Espiritu).

https://doi.org/10.1016/j.bioactmat.2021.11.035
Received 8 September 2021; Received in revised form 12 November 2021; Accepted 28 November 2021
Available online 6 January 2022

Abbreviations

AP	Anterior/Posterior
ASTM	American Society of Testing and Materials
B 0	Main Magnetic Field
DICOM	Digital Imaging and Communications in Medicine
FOV	Field of View
GRE	Gradient Echo
HF	Head/Foot
LR	Left/Right
Mg MRI	Magnetic Resonance Imaging
ORTH	Orthogonal
PAR	Parallel
RF	Radio Frequency
SAG	Sagittal
TAV	Total Artefact Volume
TE	Echo Time
Ti	Titanium
tp	Time Point
TR	Repetition Time
TRA	Transverse
TSE	Turbo Spin Echo
w	Weighted

radiation in serial CT examinations adds to the cumulative radiation dose of patients which may be associated with a small but significantly increased risk of malignancy [10]. Since MRI does not administer any type of ionising radiation, long-term harmful effects are considered insignificant [11]. However, diagnostic imaging quality can be compromised by image artefacts attributed to the patient (motion and flow artefacts), signal processing (wrap around and chemical shifts), or to the hardware (static magnetic field or radiofrequency (RF) transmission field inhomogeneities).

In MRI metallic implants may cause image distortion artefacts, or susceptibility artefacts. Metals have intrinsic magnetic susceptibilities that produce significant local field disturbances. These local changes in the resonance frequency shift image pixels away from their true positions leading to significant geometric distortions including signal reduction or voids (black areas in the image) and signal enhancements (bright areas in the image). These distortions are created by perturbations of the static magnetic field and are related to the specific material properties of the implant. Although there have been many methods demonstrating a reduction in artefacts [12], complete metallic artefacts cannot be removed.

Metallic implants made of materials, like Mg, have shown to cause image artefacts due to the inherent magnetic susceptibility of the material. However, their impact on MRI quality is less compared to other current permanent metallic implants [13].

The evaluation of artefact production in MRI is necessary when choosing a biomaterial. Artefact limitation is vital since compromised or poor image quality may disturb medical diagnosis or anatomical visualisation. The aim of this investigation is to quantify the metallic artefact production of Mg-based implants during the degradation process in various MRI settings with the ultimate goal to support the use of Mg-based implants in the clinical setting due to successful visualisation in MRI. To benchmark the MRI performance of Mg-based implants standard, commercial Ti based implants are used as a reference.

2. Materials and methods

2.1. In vitro investigation

Orthopaedic compression screws 40 mm in length and diameter of 3.2 mm made of WE43-based material manufactured by Syntellix AG (Hannover, Germany) underwent *in vitro* degradation. The volume of the WE43 screw is 151.51 mm^3 with a surface area of 552.54 mm^2. Chemical composition of WE43 includes Yttrium (3.7–4.3%), Rare Earth Elements (2.4–4.4%), Zirconium (0.4%), with the remainder composing of Mg [14]. A non-degraded WE43 screw and a titanium equivalent of similar geometry were included for comparative results (Fig. 1).

The WE43 samples were degraded via a modified ASTM F3268 Standard [15] with Dulbecco's Phosphate Buffered Saline (DPBS). A total of five screws were degraded in the DPBS with different immersion times varying by one week with a total of five time points (1 week, 2 weeks, 3 weeks, 4 weeks, and 5 weeks). After immersion time was completed, the samples were cleaned with distilled water to remove any excess salts and rinsed with ethanol to prevent further oxidation before drying and storage.

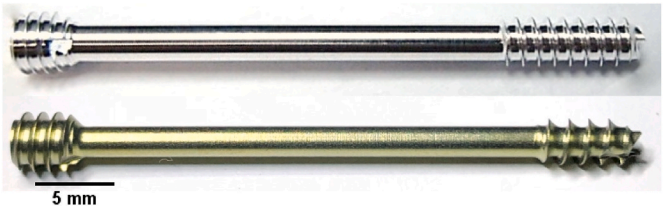

Fig. 1. 40 mm Mg-based orthopaedic compression screw MAGNEZIX® CS ø3.2 (top) and Ti market-equivalent (bottom).

For the in vitro MRI measurements, a 1.5 T (GE Signa Artist, GE Healthcare, Waukesha, USA), 3.0 T (Skyra Fit, Siemens, Erlangen, Germany) and 7.0 T (Magnetom, Siemens, Erlangen, Germany) MRI Scanner were used. Further details on the imaging protocol and imaging techniques employed for the *in vitro* measurements are documented in Table 1.

The following *in vitro* procedure has been adapted from ASTM F2119 [16] and consists of two parts: (1) the acquisition of images with the test object's long axis perpendicular to the main magnetic field (B_0), and (2) the acquisition of images with the test object's long axis parallel to the main magnetic field. Implant orientation relative to the main magnetic field, imaging sequence applied, slice orientation, phase-encoding direction, and material were varied for each combination before each image acquisition. The test object was suspended in a home built phantom acrylic container via a 3D printed holder filled with $CuSO_4$ solution (Merck Millipore, USA) to reduce T_1 relaxation effects. Artefact dimensions were determined by applying the ASTM F2119 definition for artefacts via a custom MATLAB (The MathWorks Inc., USA) script. Examples of measurements completed by the script are shown in Fig. 2. The diameter artefact is measured by determining the longest artefact along the diameter of the screw. The length artefact is determined by measuring the longest artefact along the length of the screw. The largest

Table 1
Parameters of sequences used for *in vitro* MRI investigations.

B_0 Field Strength [T]	1.5		3.0		7.0	
RF Coil Type	Spinal		Spinal		Basic Volume	
Sequence	GRE	TSE	GRE	TSE	GRE	TSE
TR [ms]	100	500	500	1190	550	1190
TE [ms]	15	20	13	20	13	30
FOV [mm]	300	300	180	200	185	185
Matrix Size [pixel]	256	256	256	256	256	256
Slice Thickness [mm]	2	2	2	2	2	2

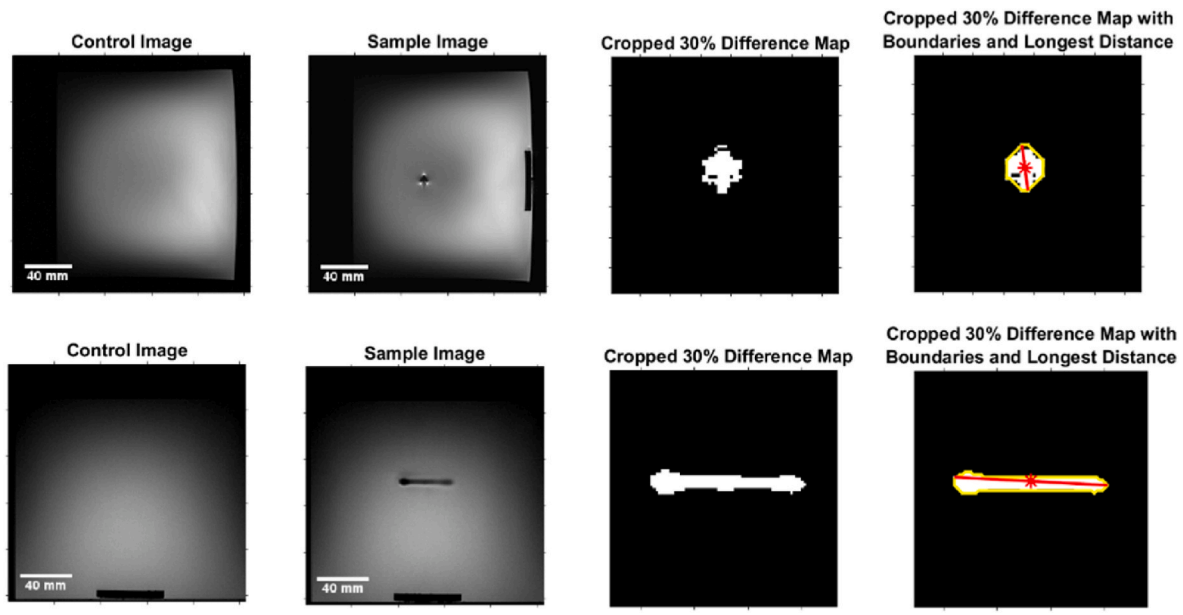

Fig. 2. Script workflow of diameter (to p) and length (bottom) artefact measurement of image data acquired at 3 T MRI. A control and a sample image are loaded and compared to detect a 30% intensity change. This change is used to create a binary image where a longest distance can then be measured (red indicator line).

measurements are taken as the 'worst-case' artefact.

Calculation of test object distortion was performed to determine the artefact size in relation to the test object dimension. Test object distortion is calculated by:

$$\frac{\textit{Total artefact length measured} - \textit{test object dimension}}{\textit{Test object dimension}}$$

2.2. Ex vivo investigation

2.2.1. Experimental animals

All *in vivo* experiments were carried out in accordance with the National Ethical Guidelines (Italian Ministry of Health; D.L.vo 26/2014) and the guidelines from Directive 2010/63/EU of the European Parliament. The protocol was approved by the Instituto Superiore di Sanità on behalf of Italian Ministry of Health and Ethical Panel (Prot. n° 299/2020-PR) and the local ethics committee. Additionally, the protocol conformed to the ARRIVE guidelines [17].

A total of three 12-week-old female Wistar rats were used in this experiment. On surgery, animals were anesthetized with an intraperitoneal injection of 5 mg/kg Xylazine (Rompum Elanco, Italy) and 10 mg/kg Zoletil (Virbac, Switzerland). The depth of anaesthesia was controlled by toe pinch response.

2.2.2. Surgical approach

Through a lateral approach, an incision was made on the skin and the muscles are carefully teased away to expose the mid-diaphyseal region of the femur. A drill with 1.55 mm diameter is used to prepare the transcortical implantation bed with the longitudinal axis of this drill perpendicular to the longitudinal axis of the femoral diaphysis. Drilling is performed at low rotational speed and profuse physiological saline (Fresenius Kabi, Italy) irrigation is applied via syringe to minimise frictional heat and thermal necrosis. A pin implant of 8 mm in length and 1.5 mm in diameter made of WE43 or Ti was implanted in this procedure. The cylindrical implant is inserted by gentle tapping, resulting in a uniform press fit. After transcortical placement is ensured, the operating field is cleaned with sterile cotton tips for remaining bone debris and the wound is closed with resorbable sutures (Johnson & Johnson Medical, Italy). Thereafter, the contralateral side is operated in the same way and using the same implant type.

The sacrifice of the animals at various time-points is performed with a lethal dose of isoflurane (IsoFlo, Zoetis, Italy); hind paws are explanted cutting through the hip joint and stored at −20 °C until further analysis.

2.2.3. Explant imaging

The explants were scanned to obtain information on the influence of hard and soft tissue on the artefact production, moving closer to mimicking the true physiological environment. *Ex vivo* MRI measurements of the hind paws were performed at Consiglio Nationale delle Ricerche Area della Ricerca di Pisa (Pisa, Italy) using a 7 T small animal MRI scanner (Bruker Avance III HD 300). Further details and sequences employed for measurements are documented in Table 2.

DICOM images were loaded and analysed with MATLAB. The artefact area of each scan was measured within each sequence set for one explant containing a WE43-based pin one day after surgery, one explant containing a WE43-based pin thirty days after surgery, and one explant containing a Ti-based equivalent. A single time-point was selected for Ti since the material is not expected to degrade, unlike the WE43 material. A total of 18 tracings were completed (six tracings per sample). To calculate the total artefact volume (TAV) for each scan, the artefact areas measured for each slice were summed and multiplied by the slice thickness as described by the Debatin method [18].

2.3. Clinical investigation

2.3.1. Clinical trial

Imaging data in humans was provided by the randomised controlled clinical trial SCAMAG (Comparison of scaphoid fracture osteosynthesis

Table 2
MRI sequences applied during explant imaging at 7 T.

B_0 Field Strength [T]	7.0
RF Coil	Quadrature Bird Cage
Sequence	T1 RARE
TR [ms]	1500
TE [ms]	7
Spatial resolution [mm]	0.12
FOV [mm]	30
Matrix Scan [pixel]	256
Slice Thickness [mm]	0.8

by magnesium-based headless Herbert screws with titanium Herbert screws) [19]. The trial is a blinded observer controlled parallel two-group post-market trial with a follow-up of one year per patient. Each involved patient is treated with either a Ti or Mg-based compression screw. The primary aim of SCAMAG is to demonstrate Mg-based compression screws as non-inferior when compared to Ti in the treatment of scaphoid fractures. The study protocol adheres to the SPIRIT [20] and CONSORT [21] statements. The SCAMAG trial was approved by the ethics committee of the Hanover Medical School (MHH) on September 27, 2017 (registration number: 7614) including registration with the German Register for Clinical Trials (DRKS, drks.de) on December 4, 2017 (registration number: DRKS00013368).

2.3.2. Patient imaging

Randomly chosen patients involved in the study treated with Mg-based compression screw (MAGNEZIX® CS, Syntellix AG, Hannover, Germany) participated in MRI examinations. The scans were performed on a 3 T MR scanner (Vario, Siemens, Erlangen, Germany) at the Medical School Hannover (Hannover, Germany). Typical wrist imaging MRI protocols were performed for this study, which are summarised in Table 3.

DICOM images were loaded and analysed with MATLAB R2019b (The MathWorks Inc., US). A total of four patient follow-up scans were included in this analysis. The first, second, third, and fourth patients were treated with a single compression screw of sizes Ø 2.7 mm with length 26 mm, Ø 3.2 mm with length 26 mm, Ø 3.2 mm with length 20 mm, Ø 3.2 mm with length 24 mm, respectively. The artefact area of each scan was measured within each sequence set for the available time points: 1.5-, 3-, 6-, and 12-months post operation. A total of 64 tracings were completed. The TAV was calculated similarly as in Section 2.2.

2.4. Statistics

Statistical analyses were performed using RStudio (RStudio, USA). A p-value of <0.05 was chosen to be statistically significant.

To compare the artefacts produced by Ti, Mg, and various time-corroded Mg samples in the *in vitro* measurements with respect to implant orientation, sequence type, slice orientation, and encoding direction, an analysis of variance (ANOVA) was completed. If a significant p-value was determined, pairwise comparisons were performed using a Tukey's post hoc multiple comparison procedure.

For *ex vivo* investigations, the ANOVA test was applied to determine differences between material implanted into the rat femur. The ANOVA test was also applied in the clinical cases to determine the significant effects of slice orientation and healing time on the TAV.

Table 3
MRI scanning protocols from SCAMAG clinical trial. Scanning sequences used include proton density-weighted turbo spin echo with fat saturation (PDw TSE with FS) and T1/T2-weighted turbo spin echo (T1/T2w TSE).

Field Strength [T]	3.0			
Sequence	PDw TSE with fat saturation	T1w TSE	T2w TSE	T2w TSE
Slice Plane	Axial	Coronal 1	Coronal 2	Sagittal
TR [ms]	3220–4290	485–586	3090–3160	2430–2920
TE [ms]	37	32	39	97
Spatial resolution [mm]	0.22	0.20	0.25	0.25
FOV [mm]	100 × 80	100 × 80	100 × 80	100 × 80
Slice Thickness [mm]	2	2	2	2

3. Results

3.1. In vitro results

3.1.1. Titanium vs magnesium

By varying different MRI scanning parameters (seen in Fig. 3) the significant differences were found for the Ti and Mg samples. For all main field magnetic strengths, the Mg-samples produced significantly less artefacts than the Ti counterparts. Turbo spin echo sequences produced lower artefacts versus gradient echo sequence. The averaged diameter- and length-measured artefacts are summarised in Table 4. Averaged distortions or artefact measured based on material and magnetic field strength are documented in Fig. 4. An increase in magnetic field strength results in an increase in artefact size for both materials. The application of the gradient echo sequence and use of Ti material generally produced higher distortions than the turbo spin echo sequence and the use of Mg with the exception of the PAR-TSE-TRA-AP/LR protocol at 3.0 T and 7.0 T of the PAR-TSE-SAG-AP protocol at 7.0 T. The Tukey post-hoc test revealed significant pairwise differences between the artefacts size obtained at 1.5 T and 7 T and at 3 T versus 7 T. No significant difference in artefact size was found between 1.5 T and 3 T. The p-values of parameters changed in this investigation are listed in Table 5.

3.1.2. The influence of Mg in vitro corrosion time on artefact production

Examining the effect of the Mg implant corrosion time on the artefact size revealed statistically significant results (Table 6). For all magnetic field strengths a general decrease of image distortion was found for increasing *in vitro* corrosion times of the implant (Fig. 5).The spin echo sequence produced lower artefacts than the gradient echo sequence (Fig. 6).

3.2. Ex vivo results

Fig. 7 illustrates MR images obtained for rat explants with Mg and Ti pins using the small bore animal 7 T MRI scanner. Ti produced higher distortion of approximately 3 times more TAV than the Mg-based samples ($p < 0.05$) when scanned with the Turbo RARE sequence. TAV averaging highlighted in Fig. 8 indicates a very minor decrease in TAV from one day to thirty days of the Mg samples post-surgery, although not significant. The implantation of the pin into the femur with hard tissue (bone) and soft tissue (muscle) disturbs the anatomic integrity of the images by introducing artefacts as illustrated in Fig. 7.

3.3. Clinical results

Fig. 9 shows a decrease in the hypointense area surrounding the implant after one month, three months, and twelve months post-surgery for a single patient. The rest of the patient data follows a comparable trend (Fig. 10). Significant differences were found between healing times and imaging slice positions. An increase in implant degradation and patient healing time resulted in a decrease in artefact production. Imaging the implant at 1.5 months with a T2w TSE sequence in the sagittal direction produced the largest TAV of approximately 650 mm^3. Since the screw is implanted into the scaphoid bone, the shape of the implant in Fig. 9 is defined since it is primarily surrounded by one type of material, spongy bone.

4. Discussion

Postoperative care in the field of orthopaedic surgery relies heavily on precise imaging techniques. Early-stage research of biomaterials concentrates on the assurance of appropriate mechanical and physiological responses between the host and the implant. Further along a product's developmental stage requires insight on product application and translational aspects. Medical imaging compatibility is one of the

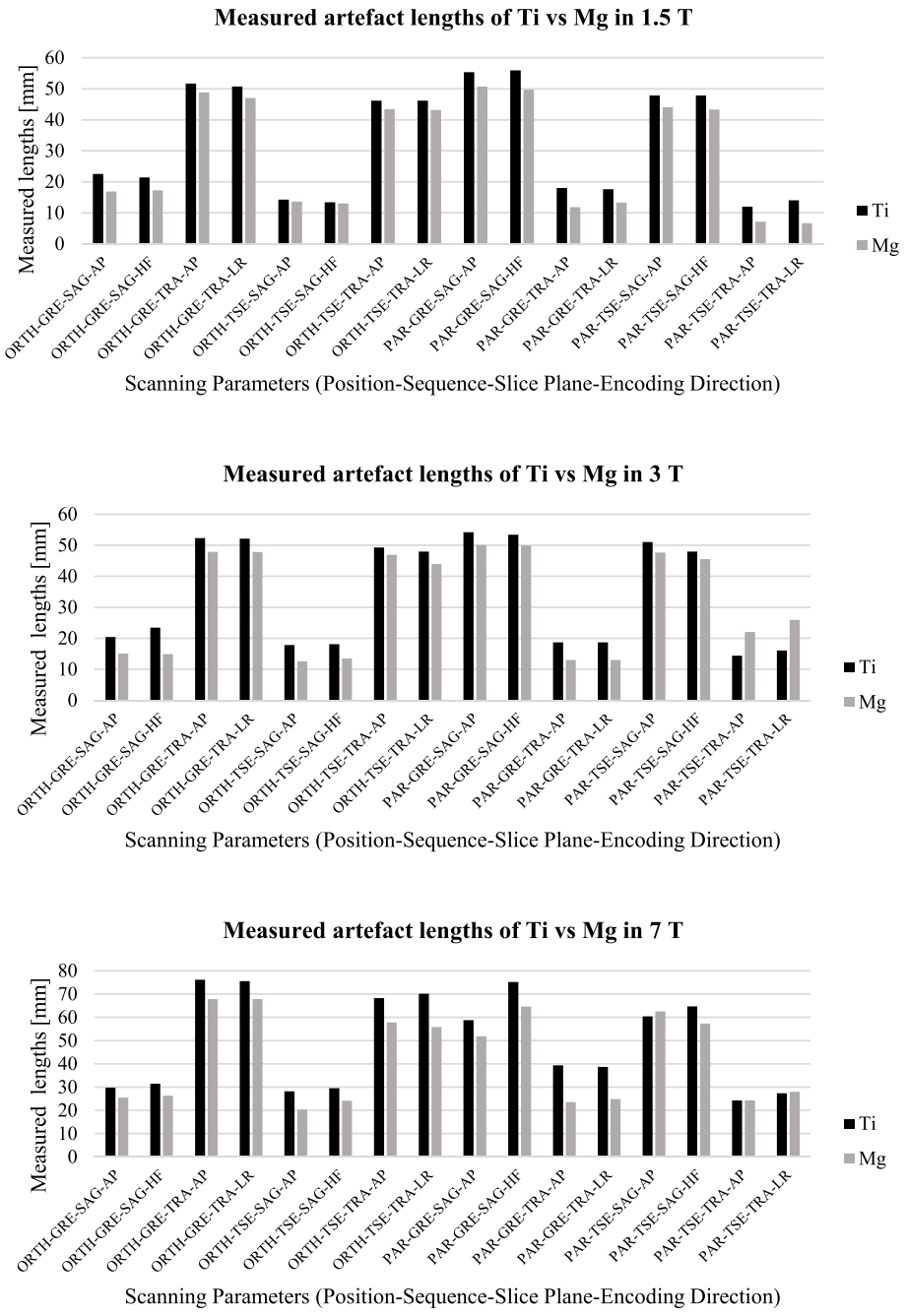

Fig. 3. Measured artefact lengths of Ti and Mg in various magnetic strengths. Implant position relative to the main magnetic field, sequence applied, slice plane, and phase encoding direction were altered for artefact measurements. (Reading format of y-axis: IMPLANT POSITION-SEQUENCE-SLICE PLANE-ENCODING DIRECTION).

Table 4
Average measured metallic artefact of Ti and Mg in MRI along the diameter and length of the implant.

B_0 Field Strength [T]	1.5		3.0		7.0	
Material	Ti	Mg	Ti	Mg	Ti	Mg
Average Diameter [mm]	16.7 ± 3.9	12.5 ± 3.9	18.5 ± 2.7	16.2 ± 5.0	31.1 ± 5.3	24.6 ± 2.2
Average Length [mm]	50.2 ± 3.9	46.3 ± 3.2	51.0 ± 2.4	47.5 ± 2.1	68.7 ± 6.9	60.7 ± 5.9

many focusses. The artefact production of an implant material may sometimes be overlooked but is a key property of the material and must be considered during a product's design process. Previous studies have documented artefact behaviour of magnesium-based implants in MRI [22–24]. Our study is the first which reports on the assessment of artefact behaviour of WE43-based implants in *in vitro, ex vivo,* and clinical environments. Our work adds to the literature by examining the impact of the magnetic field strength on the artefact behaviour. More importantly, our study provides clinically meaningful insights on how degradation time affects artefact behaviour for the experimental setups used in this work.

A well-known and commercially equivalent orthopaedic implant material like Ti is widely used today [25]. With research and popularity

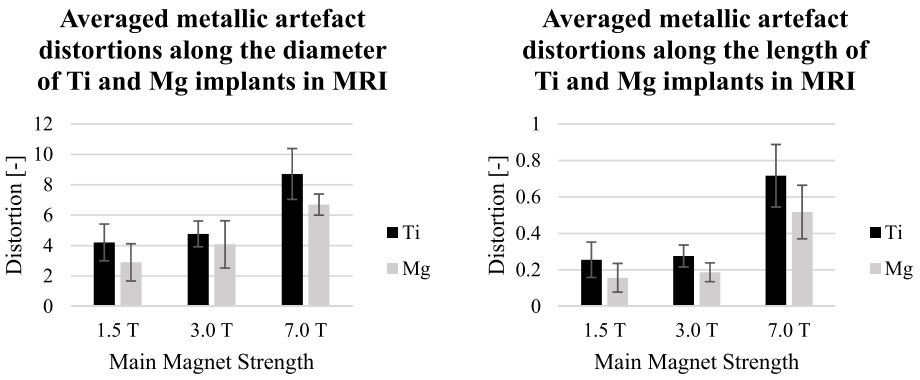

Fig. 4. Averaged artefact distortions of diameter (left) and length (right) measurements of Ti and Mg in MRI.

Table 5
ANOVA and post hoc significance of varied parameters on metallic artefact produced by Ti vs Mg in MRI. Encoding directions are abbreviated as follows: anterior/posterior (AP), head/foot (HF), and right/left (RL).

Parameter	Diameter p-value	Length p-value
B_0 Magnetic Strength	<0.05	<0.05
3 T:1.5 T	0.11	0.73
7 T:1.5 T	<0.05	<0.05
7 T:3 T	<0.05	<0.05
Implant Position	0.68	0.57
Imaging technique (GRE:TSE)	<0.05	<0.05
Phase Encoding Direction	0.62	0.47
HF:AP	0.77	0.67
RL:AP	0.66	0.99
RL:HF	0.98	0.70
Material	<0.05	<0.05

Table 6
ANOVA and post hoc significance of varied parameters on metallic artefact produced by corroded Mg samples for different time points (tp). Encoding directions are abbreviated as follows: anterior/posterior (AP), head/foot (HF), and right/left (RL).

Parameter	Diameter p-value	Length p-value
B_0 Magnetic Strength	<0.05	<0.05
3 T:1.5 T	<0.05	0.40
7 T:1.5 T	<0.05	<0.05
7 T:3 T	<0.05	<0.05
Implant Position	0.60	0.13
Imaging Technique (GRE:TSE)	<0.05	<0.05
Encoding Direction	0.44	0.12
HF:AP	0.51	0.54
RL:AP	0.61	0.82
RL:HF	0.99	0.32
Corrosion Time	<0.05	<0.05
1tp:0tp	0.24	0.98
2tp:0tp	0.21	0.61
3tp:0tp	<0.05	0.11
4tp:0tp	<0.05	0.05
5tp:0tp	<0.05	<0.05
2tp:1tp	0.98	0.95
3tp:1tp	0.98	0.43
4tp:1tp	0.47	0.26
5tp:1tp	0.08	<0.05
3tp:2tp	0.99	0.91
4tp:2tp	0.51	0.79
5tp:2tp	0.09	0.24
4tp:3tp	0.89	0.99
5tp:3tp	0.35	0.82
5tp:4tp	0.94	0.94

of magnesium-based implants increasing, a comparison between the two materials is conceptually appealing. Our findings demonstrate that the Mg-based material outperforms Ti in the *in vitro* environment by producing lower metallic distortion artefacts. Magnetic field perturbations are present around metallic objects in MRI which leads to a modification of hydrogen nuclei precession rates. The change in precession rates results in signal losses or pixel shifts and may manifest in local hypointensities or hyperintensities in MR images. Magnetic field variations are dependent on the magnetic susceptibility of the implant and the surrounding environment (in our case a $CuSO_4$ solution). Since the difference between the magnetic susceptibility of Ti and $CuSO_4$ is pronounced versus the difference between Mg and $CuSO_4$, larger magnetic field distortions are to be expected around a Ti implant.

When introducing corrosion time as a parameter, a decrease in artefact production is noticed as the implant is degraded *in vitro*. As Mg degrades in the body, the base metallic material corrodes forming non-metallic degradation layers composing mainly of MgO and $Mg(OH)_2$ [26]. As such, the base metallic material begins to shrink in volume resulting in a reduced artefact size. This decrease in artefact size is confirmed by our results obtained for a range of *in vitro* corrosion times. The question of how the degradation layer affects artefact production can be answered by analysing the magnetic properties of the degradation layer. Mainly composing of $Mg(OH)_2$ [27], the degradation layer consists of diamagnetic material. As *in vivo* degradation occurs, calcium and magnesium apatite corrosion products additionally form [28]. However, since calcium phosphates are intrinsically diamagnetic, these compounds are trivial with respect to magnetic field interference. Thus, the degradation layer dampens the effects of magnetic field variations caused by the base metallic material. This layer has been reported to be on the micrometer scale [29], which may be assumed to have an almost negligible damping effect.

Standards and norms governed by global organisations, such as ASTM F2119, are referred to by regulatory bodies to ensure patient safety and quality control. Our *in vitro* investigations, based on the ASTM F2119 standard, also considered how parameters such as implant position, encoding direction, and imaging techniques affected artefact production. Of the three, the only parameter that significantly affected artefact production was the MR imaging technique used. In both *in vitro* investigations, GRE imaging generally produced larger artefact size versus fast spin-echo imaging. Spin echo based imaging techniques are less affected by susceptibility artefacts than gradient echo techniques because of the use of a train of refocusing pulses that helps to partially compensate for dephasing of spins caused by metallic objects. Additionally, imaging the diameter of the screw produced larger artefact size than imaging the length of the screw.

Our results add to the literature by providing important insights on how the main magnetic field strength of an MRI system contributes to metallic artefact production. An early study by Ludeke et al. describe show the magnitude of susceptibility artefacts increases with magnetic field strength [30]. This relationship is exemplified in Figs. 4 and 5 where an increase of distortion was observed when moving from 1.5 T to 3.0 T and 7.0 T. It should be noted that conductive implants interact

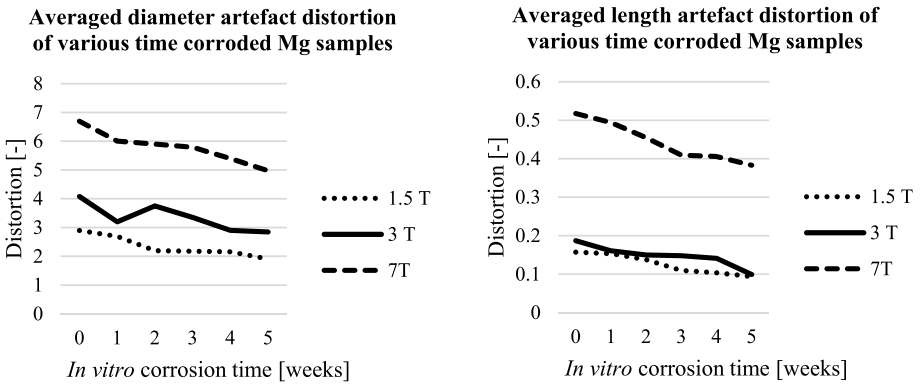

Fig. 5. Averaged diameter (left) and length (right) artefact distortions of Mg-based samples as a function of *in vitro* corrosion time.

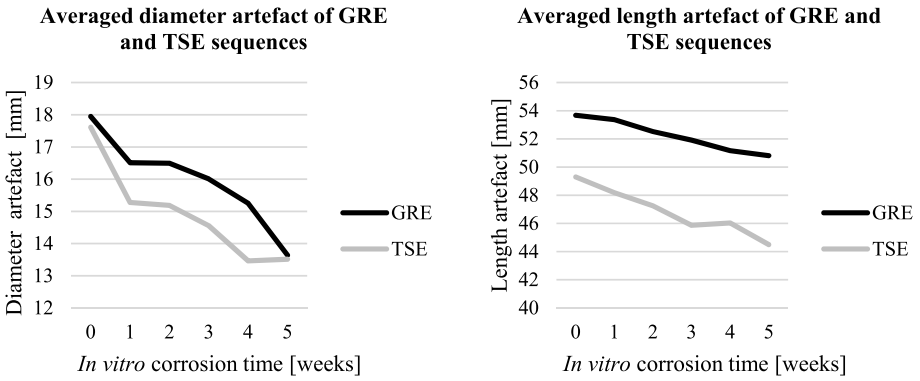

Fig. 6. Averaged diameter (left) and length (right) measured artefacts of Mg-based samples as a function of *in vitro* corrosion time and scanning sequences.

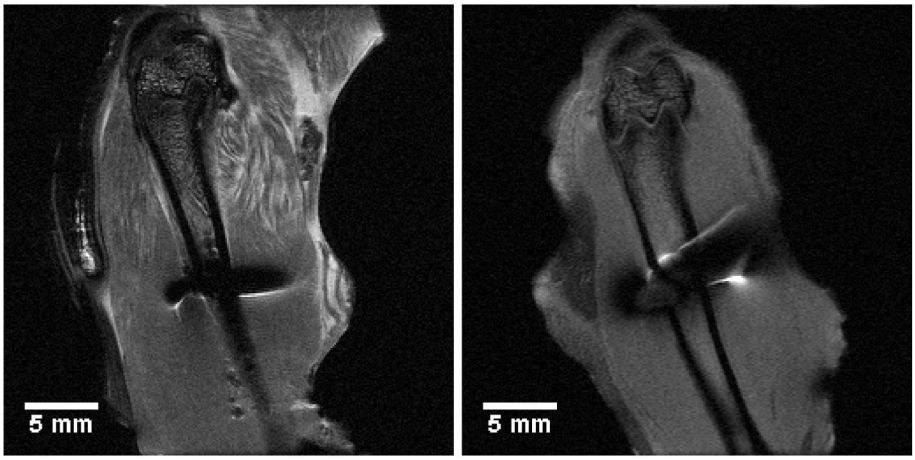

Fig. 7. Example of T1-weighted images of rat femur explants with WE43 and Ti pins implanted transcortical to bone.

with radio frequency (RF) signals from MRI transmitters. These interferences may cause extra artefacts and may even elevate local RF power deposition and energy absorption in the neighbouring region of the implants which may exceed regulatory limits and RF exposure guidelines [31,32].

Explants analysed in this investigation underwent freezing at −20 °C and thawing before scanned in a small animal 7.0 T MRI system. MRI availability could not be synchronised with the euthanasia of the animals and therefore animals needed to be stored. The freezing and thawing cycle has shown to effect MRI by significantly reducing the effective transversal relaxation time T_2* [33]. Such an effect should be considered when interpreting the results. However, the motivation behind our explant analysis is to provide insights into artefact production in hard and soft tissue. Although there were no significant differences obtained for the WE43 samples at different time points, Ti showed an approximately three times larger TAV than the WE43 material.

The clinical results and analysis revealed important information on artefact production of Mg-based implants used to treat scaphoid fractures. Averaging measurements of the four patients included in this investigation followed a similar trend of artefact reduction with patient healing time. The decrease in distortion also provides proof of implant degradation or a loss of metallic base material. More importantly, after averaging all patients and artefacts derived for each imaging plane, an extrapolation of the healing time can be made until the artefact size

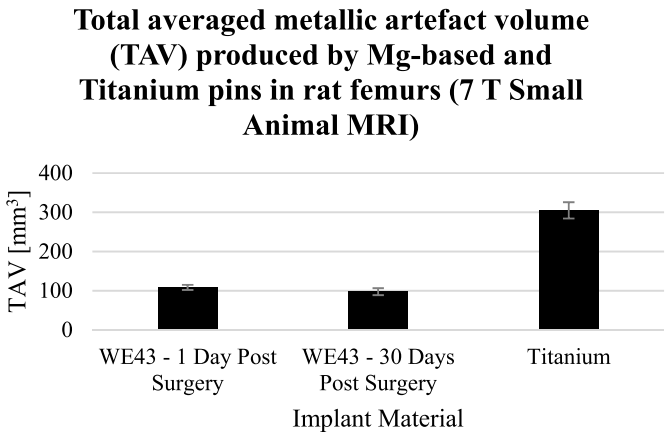

Fig. 8. Total averaged artefact volume produced by pins implanted into rat femurs imaged in 7 T small animal MRI.

reaches zero. Although this extrapolation has limitations (such as implant size), complete disappearance of artefact is approximately reached at 2.1 years, which is in accordance with a one-to-three-year implant resorption period [4,34,35]. Many methods have been employed to track implant degradation rates *in vitro* and *in vivo*, such as computed tomography segmentation and hydrogen gas release [36]. The reduction in metallic artefact size measured in MRI with progressing degradation may offer a viable alternative for screw degradation monitoring and tracking.

This investigation utilised two parameters to quantify artefact production caused by the Mg-based and Ti implants. Distortion quantifications were employed in the *in vitro* measurements while total artefact volume (TAV) was employed in the *ex vivo* and clinical analysis. The inclusion of two measurement methods was chosen to describe the artefact production behaviour of the implants in more than one way. Analysing the two measured quantities show an agreement in the decline of metallic distortion trend of Mg during the degradation process.

Metal artefact reduction techniques are widely used today to negate the effects of metallic implants in MRI [37]. Various specialised software and MRI vendors provide dedicated imaging techniques tailored for reducing metallic artefacts. Since these approaches vary from MRI vendor to vendor, our study excluded their impact as it is out of the scope of this study. However, the literature reports that some metal artefact reduction techniques do not produce statistically significant results when applied to Mg [24]. Examining the efficacy of these metal artefact reduction techniques on Mg-based material warrants further investigation.

A limitation of the *in vitro* aspect of this study is found in the natural behaviour of Mg itself. The inherent corrosion process of the implants made it impractical for samples to be tested more than once due to the interaction with $CuSO_4$ solution. Regarding explant analysis, the movement of blood is avoided in the *ex vivo* animal studies so that blood motion artefacts are eliminated. An increase in explant samples and clinical patients would enhance the statistical power of our findings.

Future studies should include the examination of different animal models to gain insights for other orthopaedic applications or solutions. Alternative *in vitro* implant degradation methods can be used to mimic specific environments. These methods should also be analysed to investigate how the degradation method affects artefact production. Furthermore, the inclusion of multi-modal data such as clinical computed tomography can be explored in quantifying an implant volume to MRI artefact production ratio.

Assessing the artefact production behaviour of Mg-based implants *in vitro, ex vivo,* and in clinical application provides valuable insights into the material's properties and its implications for MRI image quality. Our results demonstrate that Mg-based implants displayed a decrease in metallic artefact production with implant degradation. As the implant degrades and artefact production decreases, better visualisation of bone healing is achieved. To summarise, the Mg-based implant outperformed the Ti material by inducing lower artefact size.

5. Conclusion

In this investigation, *in vitro, ex vivo,* and clinical studies demonstrate a reduction in artefact size with implant degradation time for Mg-based screws. The largest artefact behaviour or "worst-case" scenario caused by the WE43 implants were found when imaging the non-degraded state in the *in vitro* and *ex vivo* experiments. In the clinical study, the largest

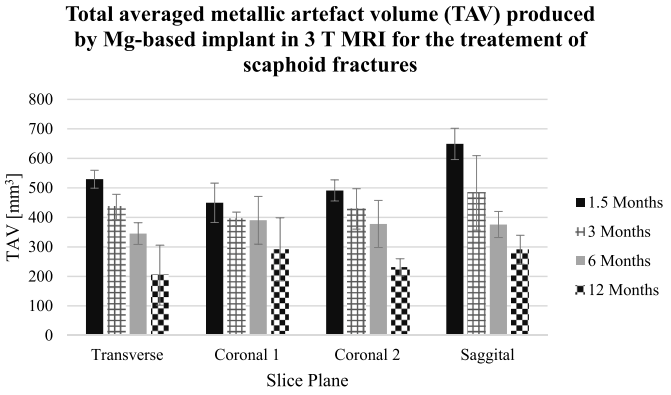

Fig. 10. Total artefact volume produced by Mg-based implant as a function of healing time in different slice planes in 3 T MRI.

Fig. 9. T2-weighted images of scaphoid with Mg-based screw one (left), three months (middle), and twelve months (right) after surgery. White arrows indicate position of implant.

TAV was observed when imaging the implant at 1.5 months in the sagittal plane. When compared against Ti-based implants, the Mg-based material induces significantly lower artefacts. Translational findings from this study suggests that Mg-based implant material should be promoted for future orthopaedic solutions due to lower artefact production. Further clinical studies are required to determine degradation rates based on artefact production as an alternative approach for degradation tracking.

CRediT authorship contribution statement

Jonathan Espiritu: Conceptualization, Methodology, Software, Validation, Formal analysis, Investigation, Resources, Data curation, Writing – original draft, Visualization. **Mostafa Berangi:** Investigation, Data curation. **Christina Yiannakou:** Formal analysis, Investigation, Resources, Data curation. **Eduarda Silva:** Methodology, Resources. **Roberto Francischello:** Data curation, Resources. **Andre Kuehne:** Investigation, Data curation, Writing – review & editing, Supervision. **Thoralf Niendorf:** Resources, Writing – review & editing. **Sören Könneker:** Methodology, Resources, Data curation. **Regine Willumeit-Römer:** Conceptualization, Supervision, Project administration, Funding acquisition. **Jan-Marten Seitz:** Conceptualization, Validation, Resources, Writing – review & editing, Supervision, Project administration, Funding acquisition.

Declaration of competing interest

Authors Kuehne and Berangi are employees of MRI.TOOLS GmbH. Author Niendorf is CEO and founder of MRI.TOOLS GmbH. Syntellix AG is a medical technology manufacturer of metallic and bio-absorbable clinical implants. Authors Espiritu and Seitz are employed as Research Associate and Chief Technical Officer, respectively.

Acknowledgements

We would like to thank Eileen Höltje and Fabian Willers from Syntellix AG (Hannover, Germany) and Roman Leicht from MRI.TOOLS GmbH (Berlin, Germany) for their support with the experiments. We would also like to acknowledge the help from Petra Keilberg, Gianni Novani, Hana Hlavata, and Matteo Bianchi from the Fondazione Toscana Gabriele Monasterio Hospital (Pisa, Italy) and Luca Menichetti from the Institute of Clinical Physiology, National Research Council (Pisa, Italy) for their support. This project has received funding from the European Union's Horizon 2020 research and innovation programme under the Marie Skłodowska-Curie grant agreement No 811226.

References

[1] B. Heublein, R. Rohde, V. Kaese, M. Niemeyer, W. Hartung, A. Haverich, Biocorrosion of magnesium alloys: a new principle in cardiovascular implant technology? Heart 89 (6) (2003) 651–656.
[2] G. Marcucci, M.L. Brandi, Kyphoplasty and vertebroplasty in the management of osteoporosis with subsequent vertebral compression fractures, Clin. Cases Mineral Bone Metabol. 7 (1) (2010) 51–60.
[3] H. May, Y.A. Kati, G. Gumussuyu, T.Y. Emre, M. Unal, O. Kose, Bioabsorbable magnesium screw versus conventional titanium screw fixation for medial malleolar fractures, J. Orthop. Traumatol. 21 (9) (2020).
[4] C. Plaass, C. von Falck, S. Ettinger, L. Sonnow, F. Calderone, A. Weizbauer, J. Reifenrath, L. Claassen, H. Waizy, K. Daniilidis, C. Stukenborg-Colsman, H. Windhagen, Bioabsorbable magnesium versus standard titanium compression screws for fixation of distal metatarsal osteotomies – 3 year results of a randomized clinical trial, J. Orthop. Sci. 23 (2) (2018) 321–327.
[5] R. Biber, J. Pauser, M. Brem, H.J. Bail, Bioabsorbable metal screws in traumatology: a promising innovation, Trauma Case Rep. 8 (2017) 11–15.
[6] H. Brar, J. Wong, M. Manuele, Investigation of mechanical and degradation properties of Mg-Sr and Mg-Zn-Sr alloys for use as potential biodegradable implants materials, J. Mech. Behav. Biomed. Mater. 7 (2012) 87–95.
[7] A. Chatterjee, C. Harmath, A. Oto, New prostate MRI techniques and sequences, Abdominal Radiol. 45 (2020) 4052–4062.
[8] P. Stroman, H. Warren, G. Ioachim, J. Powers, K. McNeil, A comparison of the effectiveness of functional MRI analysis methods for pain research: the new normal, PLoS One 15 (12) (2020).
[9] C. Nunez-Peralta, J. Alonso-Perez, J. Diaz-Manera, The increasing role of muscle MRI to monitor changes over time in untreated and treated muscle diseases, Curr. Opin. Neurol. 33 (5) (2020) 611–620.
[10] D.P. Frush, K. Applegate, Computed tomography and radiation: understanding the issues, J. Am. Coll. Radiol. 1 (2) (2004) 113–119.
[11] E. Weidman, K. Dean, W. Rivera, M. Loftus, T. Stokes, R. Min, MRI saftey: a report of current practise and advancements in patient preparation and screening, Clin. Imag. 39 (6) (2015) 935–937.
[12] P.M. Jungmann, C.A. Agten, C.W. Pfirrmann, R. Stutter, Advances in MRI around metal, J. Magn. Reson. Imag. 46 (4) (2017) 972–991.
[13] J. Espiritu, M. Meier, J.-M. Seitz, The current performance of biodegradable magnesium-based implants in magnetic resonance imaging: a review, Bioact. Mater. 6 (12) (2021) 4360–4367.
[14] Azo Materials, Magnesium Elektron WE43 Alloy (UNS M18430), 18 June 2013 [Online]. Available: https://www.azom.com/article.aspx?ArticleID=9279. (Accessed 7 October 2021).
[15] ASTM International, ASTM standard F3268-18a, in: Standard Guide for in Vitro Degradation Testing of Absorbable Metals, West Conshohocken, PA, 2018.
[16] ASTM International, ASTM standard F2119-07, in: Standard Test Method for Evaluation of MR Image Artifacts from Passive Implants, West Conshohocken, PA, 2013.
[17] V. Hurst, A. Ahluwalia, S. Alam, M. Avey, M. Baker, W. Browne, A. Clark, I. Cuthill, U. Dirnagl, M. Emersion, P. Garner, S. Holgate, D. Howells, N. Karp, S. Lazic, K. Lidster, C. MacCallum, M. Macleod, E. Pearl, O. Petersen, et al., The ARRIVE guidelines 2.0: updated guidelines for reporting animal research, PLoS Biol. 18 (7) (2020).
[18] J.F. Debatin, S.N. Nadel, H. Sostman, C. Spritzer, A.J. Evans, T.M. Grist, Magnetic resonance imaging—Cardiac ejection fraction measurements, Invest. Radiol. 27 (3) (1992) 198–203.
[19] S. Könneker, K. Krockenberger, C. Pieh, C. von Falck, B. Brandewiede, P. Vogt, M. Kirschner, A. Ziegler, Comparison of SCAphoid fracture osteosynthesis by MAGnesium-based headless Herbert screws with titanium Herbert screws: protocol for the randomized controlled SCAMAG clinical trial, BMC Muscoskel. Disord. 20 (2019) 357.
[20] A. Chan, J. Tetylaff, D. Altman, A. Laupacis, P. Gotzsche, K. Krleza-Jeric, A. Hrobjartsson, H. Mann, K. Dickersin, J. Berlin, C. Dore, W. Parulekar, W. Summerskill, T. Groves, K. Schulz, H. Sox, F. Rockhold, D. Rennie, D. Moher, SPIRIT 2013 statement: defining standard protocol items for clinical trials, Ann. Intern. Med. 158 (3) (2013) 200–207.
[21] CONSORT Group, CONSORT 2010 Statement: updated guidelines for reporting parallel group randomised trials, PLoS Med. (2010).
[22] T. Ernstberger, G. Buchhorn, G. Heidrich, Intervertebral test spacers and postfusion MRI artifacting: a comparative in vitro study of magnesium versus titanium and carbon fiber reinforced polymers as biomaterials, Open Med. 4 (4) (2009) 496–500.
[23] L. Fili, R. Luechinger, T. Frauenfelder, S. Beck, R. Guggenberger, N. Farshad-Amacker, G. Andreisek, Metal-induced artifacts in computed tomography and magnetic resonance imaging: comparison of a biodegradable magnesium alloy versus titanium and stainless steel controls, Skeletal Radiol. 44 (6) (2015) 849–856.
[24] L. Sonnow, S. Könneker, P.M. Vogt, F. Wacker, C. von Falck, Biodegradable magnesium Herbert, BMC Med. Imag. 17 (16) (2017).
[25] M.S.K. Kaur, Review on titanium and titanium based alloys as biomaterials for orthopaedic applications, Mater. Sci. Eng. C 102 (2019) 844–862.
[26] J. Seitz, R. Eifler, F. Bach, H. Maier, Magnesium degradation products: effects on tissue and human metabolism, J. Biomed. Mater. Res. 102 (10) (2014) 3744–3753.
[27] R. Rettig, S. Virtanen, Composition of corrosion layers on a magnesium rare-earth alloy in simulated body fluids, J. Biomed. Mater. Res. 88A (2) (2008) 359–369.
[28] J. Seitz, R. Eifler, W. Bach, H. Maeir, Magnesium degradation products: effects on tissue and human, J. Biomed. Mater. Res. 102 (10) (2013) 3744–3753.
[29] R. Willumeit-Römer, The interface between degradable Mg and tissue, JOM 71 (4) (2019) 1447–1455.
[30] K.M. Lüdeke, P. Röschmann, R. Tischler, Susceptibility artefacts in NMR imaging, Magn. Reson. Imag. 3 (4) (1985) 329–343.
[31] International Electrical Commision, International standard, medical equipment - Part 2: particular requirements for the safety of magnetic resonance equipment for medical diagnosis, 2nd Revision, in: International Electrotechnical Commission 60601-2-33, 2002, pp. 29–31.
[32] ICNIRP, Guidelines for limiting exporsure to time-varying electric, magnetic, and electromagnetic fields (up to 300 GHz), Health Phys. 74 (4) (1998) 494–522.
[33] S.L. Pownder, P.H. Shah, H.G. Potter, M.F. Koff, The effect of freeze-thawing on magnetic resonance imaging T2* of freshly harvested bovine patellar tendon, Quant. Imag. Med. Surg. 5 (3) (2015) 368–373.
[34] H. Waizy, J. Diekmann, A. Weizbauer, J. Reifenrath, I. Bartsch, V. Neubert, R. Schavan, H. Windhagen, In vivo study of a biodegradable orthopedic screw (MgYREZr-alloy) in a rabbit model for up to 12 months, J. Biomater. Appl. 28 (5) (2013) 667–675.

[35] H. Waizy, J. Seitz, J. Reifenrath, A. Weizbauer, F. Bach, A. Meyer-Lindenberg, B. Denkena, H. Windhagen, Biodegradable magnesium implants for orthopedic applications, J. Mater. Sci. 48 (2013) 39–50.
[36] L. Liu, K. Gebresellasie, B. Collins, H. Zhang, Z. Xu, J. Sankar, Y. Lee, Y. Yun, Degradation rates of pure zinc, magnesium, and magnesium alloys measured by volume loss, mass loss, and hydrogen evolution, Appl. Sci. 8 (9) (2018) 1459.
[37] M. Reichert, T. Ai, J.N. Morelli, M. Nittka, U. Attenberger, V.M. Runge, Metal artefact reduction in MRI at both 1.5 and 3.0Tusing slice encoding for metal artefact correction and view angle tilting, Br. J. Radiol. 88 (2015) 1048.